IEEE Access
Multidisciplinary | Rapid Review | Open Access Journal

Received 1 December 2022, accepted 21 December 2022, date of publication 28 December 2022,
date of current version 10 January 2023.

Digital Object Identifier 10.1109/ACCESS.2022.3232846

RESEARCH ARTICLE

Distributed Current Source Method for Modeling of Magnetic and Eddy-Current Fields in Sensing System Design

CHUN-YEON LIN, (Member, IEEE), MEGAN TENG, AND YI-CHIN WU, (Graduate Student Member, IEEE)
Department of Mechanical Engineering, National Taiwan University, Taipei 10617, Taiwan

Corresponding author: Chun-Yeon Lin (chunyeonlin@ntu.edu.tw)

This work was supported in part by the National Science and Technology Council, Taiwan, under Grant MOST 108-2218-E-002-038-MY2 and Grant MOST 109-2628-E-002-005-MY3; and in part by the National Taiwan University under Grant NTU-CDP-109L7759, Grant NTU-CDP-110L7742, and Grant NTU-CDP-111L7719.

ABSTRACT This paper presents a distributed current source (DCS) method for modeling the eddy current (EC) fields induced in biological or non-ferrous metallic objects in two-dimensional axisymmetric and three-dimensional Cartesian coordinates. The EC fields induced in the objects, magnetic flux density (MFD) in space, and magnetic flux (MF) of the sensing coils are formulated in state-space representation. The harmonic responses of the eddy current fields and electromotive force (EMF) of the sensing coil are formulated in closed-form solutions. The proposed DCS method is applied to design two eddy current sensing systems. The Bio-Differential Eddy Current (BD-EC) sensor distinguishes biological objects, and the Metal-Coaxial Eddy Current (MC-EC) sensor classifies non-ferrous metallic objects. The simulated EC field and EMF are numerically verified by comparing results with finite element analysis. An example is utilized to illustrate the advantage of the DCS method for calculating the MFD, MF, and EMF contributed from the induced ECD in the objects directly, and the EMF generated from each material. The proposed method, along with a prototype of the BD-EC sensor, has been experimentally evaluated on sweep frequency analysis for detecting meat and bone.

INDEX TERMS Eddy currents, modeling, sensing system.

I. INTRODUCTION

Eddy current (EC) devices play a vital role in a broad spectrum of applications ranging from manufacturing to biomedical engineering. For the EC actuators in manufacturing applications, the electrodynamic bearings utilize the repulsive forces generated by eddy currents to carry the moving body passively [1]. Eddy current thrust without physical contact provides a mechanical signal proportional to speed, and the eddy current reaction force can be utilized as the eddy current speedometers for moving objects [2]. The eddy current brake is commonly used in vehicles [3]. The electromagnetic damper is employed for vibration suppression [4], and eddy currents can be utilized for induction heating for injection molding plates [5]. In biomedical engineering applications, transcranial magnetic stimulation (TMS) is a technique that uses the principle of electromagnetic induction to focus induced eddy currents in the brain for modulating cortical function and is a neuromodulation therapy to treat neurological and psychiatric conditions [6], [7], [8].

For the EC sensors in manufacturing applications, the eddy current displacement sensor is compact, robust, stable, accurate, and relatively low-cost and can be utilized for position sensing [9], [10]. The eddy current sensors are widely used in non-destructive testing, such as detecting fiber fractures [11], [12], measuring thickness [13], electrical conductivity [14], and detecting crackers [15]. In other applications, the eddy current probe can be used to detect the broken surface wires of the steel wire rope [16] and measure the extent of corrosion of sacrificial anodes used in

The associate editor coordinating the review of this manuscript and approving it for publication was Giambattista Gruosso.

cathodic protection systems for real-time monitoring of the efficiency and remaining useful life of the cathodic protection system [17].

Magnetic induction tomography (MIT) is a technique using excitation coils to induce an alternating (primary) magnetic field that induces eddy currents inside the exciting object. These currents generate their own (secondary) information about the passive electromagnetic properties, such as electrical conductivity, permittivity, and magnetic permeability. In manufacturing applications, a multi-channel MIT system is applied to identify the various sizes of cracks on carbon fiber rods [18], conductive fluid imaging [19], and molten metal flow visualization [20]. In biomedical engineering, MIT applications involve Hemorrhagic stroke detection [21], [23], lung imagining [24], and liver tissue monitoring [25]. Besides using the array of coils, the differential coil system is used to image the electrical conductivity of biological tissues via contactless measurements [26].

Modeling magnetic and eddy current fields are needed to develop the device. Dodd et al. derived analytical solutions for axisymmetric eddy currents induced in the metal plates for the metal plates [27]. The truncated region eigenfunction expansion (TREE) method utilizes the series expressions to calculate the magnetic field for multilayered conductive structures [28]. The analytical and numerical methods for modeling eddy currents generated in conducting materials by time-varying magnetic fields are reviewed in [29]. The distributed current source (DCS) method models the eddy-current field induced in the non-ferrous metal, and its corresponding magnetic flux density (MFD), which considers the boundary effects of the objects [30], and can be utilized for designing a magnetic/eddy-current sensing system [31]. The impedance method models the biological bodies exposed to time-varying electromagnetic fields in two and three dimensions using an impedance network [32], [33]. Later, the independent impedance method (IIM) improves the conditionality [34]. A combination of an OcTree type multi-level adaptive orthogonal mesh generation algorithm with a conformal finite integration technique-like formulation is utilized for solving the magnetic induction tomography forward problem [35]. Cole-Cole dispersion describes the variation of dielectric properties of tissues as a function of frequency [36], [37].

Table 1 lists the applications of the DCS method for eddy current sensor design. This paper extends the previous work to model the eddy current fields in biological objects with multiple layers and calculate electromotive force (EMF) for the sensing coils. The distributed eddy current densities of elements are formulated as the state-space representation. Further, ECDs in the objects, MFDs in space, MF of the sensing coil are formulated in the state-space representation. The closed-form solution of the harmonic responses of the ECDs in the objects and EMF of the sensing coil are derived. The DCS method can replace the analytical model and serve as the theoretical backbone with better flexibility and less restrictive assumptions.

TABLE 1. DCS method for eddy current sensor design.

	[30]	[31]	This paper
Material type	Metal	Metal	Metal/ Biological
Material number	Single	Single	Multiple
Coordinate	Axis symmetric, Three-dimensional	Axis symmetric	Three-dimensional
Sensing target	MFD	MFD	EMF

The remainder of this paper offers the following:

- A state-space model that characterizes the ECDs contributed by the electromagnet, biological/non-ferrous metallic objects, MFD in space, and MF of the sensing coil is formulated. Harmonic responses in the ECDs field of the objects and EMF of the sensing coil are expressed in closed-form solutions to investigate two designs of eddy current sensing systems.
- The DCS modeling method in three-dimensional (3-D) Cartesian coordinates is numerically investigated and verified by comparing results with the Finite Element Analysis (FEA) simulation software in two designs. An example is utilized to illustrate the advantage of the DCS method numerically.
- A prototype of the eddy current sensing system is tested on the biological objects to validate the design of the BD-EC sensor with the magnitude and phase parts in the sweep frequency response.

II. DISTRIBUTED CURRENT SOURCE METHOD FOR MODELING MAGNETIC/EDDY-CURRENT FIELDS

Fig. 1 illustrates two designs of eddy current sensors consisting of excitation and sensing coils for detecting biological and non-ferrous metallic objects. The design concept of the eddy current sensing system is that the material properties of the exciting objects are estimated by the change of the magnetic fields induced by the eddy current via measuring the EMF.

As shown in Fig. 1(a), (b), the Bio-Differential eddy current (BD-EC) sensor consists of an excitation coil and one pair of sensing coils. The small electrical conductivities of the biological tissues cause the MF generated from the biological object to be relatively small compared with MF from the excitation coil. The configuration of the differential sensing coils with opposite winding directions placed on both sides of the excitation coil cancels out the EMF generated from the excitation coil. The EMF generated from the induced eddy currents on the biological object can be detected. In addition, the metal-coaxial eddy current (MC-EC) sensor in Fig. 1(c), (d) consists of the coaxial coils, in which the outer coil is the excitation coil, and the inner coil is the sensing coil. The coaxial configuration makes the sensor more compact and close to the object.

Fig. 1(a)-(d) are the schematics of the DCS-based design for the BD-EC sensor and MC-EC in 2-dimensional (2-D)

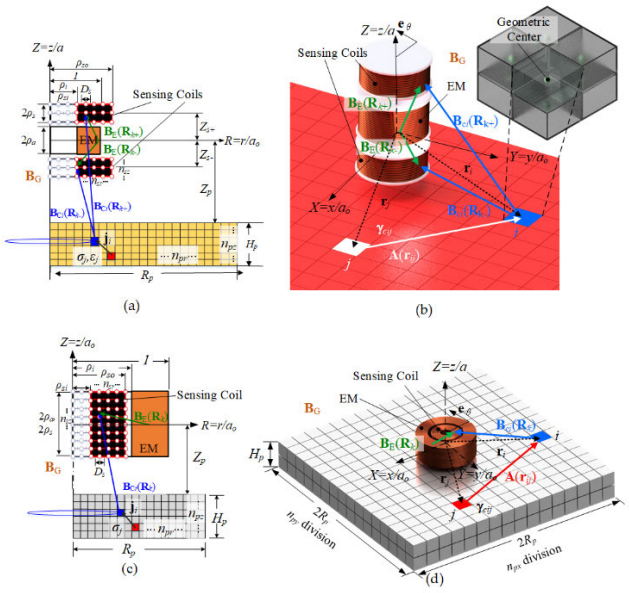

FIGURE 1. Schematics showing variables/parameters used in the magnetic/eddy-current fields modeling for sensing applications (a) Biological objects and differential coil systems in 2-D axisymmetric coordinate and (b) 3-D Cartesian coordinate. (c) Non-ferrous metallic objects and coaxial coils system in 2-D axisymmetric coordinate. (d) 3-D Cartesian coordinate.

axisymmetric and 3-D Cartesian coordinates. The inner radius, outer radius, and half-length of the excitation and sensing coils are represented by (a_i, a_o, a) and (a_{si}, a_{so}, a_s), respectively. The characteristic geometrical parameters of the sensors are normalized to a_o and a in the dimensionless form in r and z directions with normalized coordinates ($R = r/a_o$, $Z = z/a$), excitation coil ($\rho_i = a_i/a_o$, $\rho_a = a/a_o$), object ($Z_p = z_p/a$, $H_p = h_p/a$, $R_p = r_p/a_o$), and sensing coils geometry ($\rho_{si} = a_{si}/a_o$, $\rho_{so} = a_{so}/a_o$, $\rho_s = a_s/a$, $Z_{s\pm} = z_{s\pm}/a$, $D_s = d_s/a_o$). d_s is the diameter of the winding wire. As shown in Fig. 1(a), (c), the object is decomposed into square elements i ($i = 1, 2, \ldots, n_{pr} \times n_{pz}$) for modeling magnetic/eddy-current (M/EC) fields in the axisymmetric coordinate. n_{pr} and n_{pz} are the numbers of elements in the R and Z directions, respectively. The square element (surface area s_i) in the 2-D axisymmetric coordinate can be regarded as a ring element in the 3-D view. On the other hand, the cubic element (volume v_i) is utilized for the 3-D Cartesian coordinate in Fig. 1(b), (d). The discrepancy between the material properties of the biological and metal objects is the displacement currents need to be considered for the biological object, and the metal can be neglected. Each element has the material properties of σ_i, ε_i for the biological objects but the only material property of σ_i for the metallic objects. The winding elements of the sensing coil are represented by k ($k = 1, 2, \ldots n_{sr} \times n_{sz}$) in two directions.

A. EDDY-CURRENT DENSITY ON THE EXCITED OBJECT

The induced ECD field is governed by Maxwell's equation and continuity conditions in Appendix A. Using (A.9), the induced ECD of the object with electrical conductivity (σ) and permittivity (ε) are explicitly expressed in terms of MVP generated from the excitation coil/electromagnet (EM) ($\mathbf{A}_\mathrm{E}$) and mutual inductance among the conductivity element ($\mathbf{A}_\mathrm{C}$).

$$\mathbf{J} = -\left(\sigma + \dot{\varepsilon} + \varepsilon\frac{\partial}{\partial t}\right)\frac{\partial\left(\mathbf{A}_\mathrm{E} + \mathbf{A}_\mathrm{C}\right)}{\partial t} \tag{1}$$

In the 3-D Cartesian **xyz** coordinate, using (A.6) for the circular excitation coil with uniform current density, J_E flows with $\mathbf{R_i} = [R_i\cos\theta, R_i\sin\theta, Z_i]^\mathrm{T}$, $\mu_0(= 4\pi \times 10^{-7}$ H/m) is the magnetic permeability, where J_E is the amplitude of the current density for the EM, the MVP ($\mathbf{A}_\mathrm{E} = [a_{ex}, a_{ey}, a_{ez}]^\mathrm{T}$) is expressed as

$$\mathbf{A}_\mathrm{E}\left(\mathbf{r}_i\right) = \mu_o\gamma_\mathrm{E}\left(\mathbf{r}_i\right)J_E \tag{2}$$

where $a_{ek}, k \in x, y, z$ is k-component MVP. In (2), $\boldsymbol{\gamma}_\mathrm{E}$ depends on the winding geometry for an EM. In the axisymmetric coordinate, the J_E only generates in the tangential direction:

$$\boldsymbol{\gamma}_E\left(\mathbf{r}_i\right) = aa_o\left(\frac{1}{4\pi}\int_{\theta=0}^{2\pi}\int_{Z=-\rho_a}^{\rho_a}\int_{R=\rho_i}^{1}\frac{\mathbf{e}_\theta}{|\mathbf{R}_i - \mathbf{R}|}RdRdZd\theta\right)$$

where

$$|\mathbf{R}_i - \mathbf{R}| = \sqrt{(R - R_i\cos\theta)^2 + R_i^2\sin^2\theta + \rho_a^2\left(\mathrm{Z} - Z_i\right)^2}$$
$$\begin{cases}\mathbf{e}_\theta = \cos\theta & 2-\mathrm{D}\\ \mathbf{e}_\theta = -\sin\theta\mathbf{e}_\mathrm{x} + \cos\theta\mathbf{e}_\mathrm{y} & 3-\mathrm{D}\end{cases} \tag{3}$$

$\mathbf{A_c}(\mathbf{r}_\mathrm{i})$ at location i is computed from the sum of the individual MVP contributed by the n elemental ECD sources $\mathbf{j}_j$ of the j^{th} object element:

$$\mathbf{A}_\mathbf{C}\left(\mathbf{r}_i\right) = \mu_o\sum_{j=1}^{n}\left(\gamma_{cij}v_j\right)\mathbf{j}_j \tag{4}$$

γ_{cij} in (4) accounts for the mutual inductance of the cubic element for the 3D Cartesian coordinate given by [29].

$$\gamma_{cij} = \frac{1}{4\pi}\begin{cases}1/r_{ij} & i \neq j\\ \left(3r_{bi}^2 - r_{ij}^2\right)/\left(2r_{bi}^3\right) & i = j\end{cases} \tag{5}$$

where, $r_{ij} = \left|\mathbf{r}_j - \mathbf{r}_i\right|$.

In the axisymmetric coordinate, the eddy currents only generate in the tangential direction.

$$\gamma_{cij} = \frac{1}{4\pi}\int_0^{2\pi}\frac{\cos\theta}{f(\theta)}d\theta$$

where

$$f(\theta) = \begin{cases}\left|\mathbf{R}_i - \mathbf{R}_j\right| & i \neq j\\ 2\left(R_i - \cos\theta\right) & i = j\end{cases}$$
$$\left|\mathbf{R}_i - \mathbf{R}_j\right| = \sqrt{\left(R_j - R_i\cos\theta\right)^2 + R_i^2\sin^2\theta + \rho_a^2\left(Z_j - Z_i\right)^2} \tag{6}$$

Using (3), (5), and (6), which solve for the induced ECD by the EM and mutual inductances of the i^{th} cubic element in Cartesian coordinate

$$-\mathbf{j}_i = \mu_0 \left(\sigma_i + \dot{\varepsilon}_i + \varepsilon_i \frac{d}{dt}\right) \sum_{j=1}^{n} \left(\gamma_{cij} v_j \frac{d\mathbf{j}_j}{dt} + \gamma_{\mathrm{E}i} \frac{dJ_E}{dt}\right) \quad (7)$$

With $\mathbf{J} \in \mathbb{R}(\mathrm{n} \times 1) = [j_1 \ldots j_i \ldots j_n]^{\boldsymbol{T}}$ defined as the state vector and $\dot{J}_E$ as an input, (7) can be written in the matrix form.

$$-\mathbf{j}_i = \mu_0 \left[\, v_1\gamma_{ci1} \quad v_j\gamma_{cj} \cdots \quad v_n\gamma_{cin} \,\right] \times \left[\, (\sigma_i + \dot{\varepsilon}_i)\,\dot{\mathbf{j}} + \varepsilon_i \ddot{\mathbf{j}} \,\right] + \mu_0 \left[\, \left((\sigma_i + \dot{\varepsilon}_i) \quad \varepsilon_i \,\right] \boldsymbol{\gamma}_{\mathrm{E}i}\mathbf{u}$$

where,

$$\mathbf{u} = \left[\, \dot{J}_E \quad \ddot{J}_E \,\right]^{\mathrm{T}}; \quad \left[\, \mathbf{A}_{\mathrm{C}}(i,j)\right] = v_j\gamma_{cij} = v_j\gamma_{cij}$$
$$\mathbf{E_p} = diag\,(\mu_0\varepsilon_i)\,; \quad \mathbf{S} = diag\,(\mu_0\sigma_i) \quad (8)$$

(8) can be represented in the system of second-order differential equations in (9) with specified parameters,

$$\ddot{\mathbf{J}} = \boldsymbol{\alpha}_1\mathbf{J} + \boldsymbol{\alpha}_2\mathbf{J} + \boldsymbol{\beta}_1\dot{\mathbf{J}}_E + \boldsymbol{\beta}_2\ddot{\mathbf{J}}_E$$

where

$$\begin{aligned}
\boldsymbol{\alpha}_1 \left(\in \mathbb{R}^{n\times n}\right) &= -\mathbf{A}_c^{-1}\mathbf{E}_p^{-1} \\
\boldsymbol{\alpha}_2 \left(\in \mathbb{R}^{n\times n}\right) &= -\mathbf{E}_p^{-1}\left(\mathbf{S} + \dot{\mathbf{E}}_p\right) \\
\boldsymbol{\beta}_1 \left(\in \mathbb{R}^{n\times 1}\right) &= -\mathbf{A}_c^{-1}\mathbf{E}_p^{-1}\left(\mathbf{S} + \dot{\mathbf{E}}_{\mathrm{p}}\right)\mathbf{A}_{\mathbf{E}} \\
\boldsymbol{\beta}_2 \left(\in \mathbb{R}^{n\times 1}\right) &= -\mathbf{A}_{\mathbf{c}}^{-1}\mathbf{A}_{\mathbf{E}}
\end{aligned} \quad (9)$$

Further (9) can be catenated into the state-space representation in (10). The "diag" denotes a diagonal matrix with scalar elements ($i = 1, \ldots, n$) with the state vector $\mathbf{X}_\ell, \ell \in x, y, z, \phi$. For 3-D coordinate, $\mathbf{X}_x$, $\mathbf{X}_y$, $\mathbf{X}_z$ contain the x, y, and z-component eddy currents and the derivatives. For the axisymmetric coordinate, $\mathbf{X}_\phi$ is the tangential directional eddy currents. $\mathbf{U}$ is the input vector involving the current densities of the excitation coil and first and second derivatives.

$$\dot{\mathbf{X}}_\ell = \begin{bmatrix} \mathbf{0}_{n\times n} & \mathbf{1}_{n\times n} \\ \boldsymbol{\alpha}_1 & \boldsymbol{\alpha}_2 \end{bmatrix} \mathbf{X}_\ell + \begin{bmatrix} \mathbf{0}_{n\times 1} & \mathbf{0}_{n\times 1} & \mathbf{0}_{n\times 1} \\ \mathbf{0}_{n\times 1} & \boldsymbol{\beta}_1 & \boldsymbol{\beta}_2 \end{bmatrix} \mathbf{U} \quad (10)$$

where, $\mathbf{X}_\ell \left(\in \mathbb{R}^{2n\times 1}\right) = \begin{bmatrix} \mathbf{J}_\ell \\ \dot{\mathbf{J}}_\ell \end{bmatrix}$; $\mathbf{U}\left(\in \mathbb{R}^{3\times 1}\right) = \begin{bmatrix} J_E \\ \dot{J}_E \\ \ddot{J}_E \end{bmatrix}$

B. MAGNETIC FLUX DENSITY IN SPACE, MAGNETIC FLUX OF THE SENSING COIL

As shown in Fig. 1, the combined MFD ($\mathbf{B}$) measured at the sensing coil is equal to the sum of the excitation ($\mathbf{B}_{\mathrm{E}}$), eddy currents on the object ($\mathbf{B}_{\mathrm{C}}$), and the environment ($\mathbf{B}_{\mathrm{G}}$):

$$\mathbf{B} = \mathbf{B}_{\mathrm{C}} + \mathbf{B}_{\mathrm{E}} + \mathbf{B}_{\mathrm{G}} \quad (11)$$

By applying Biot-Savart law in (A.7) on the distributed elements and for the 3D Cartesian coordinate, the MFD contributed by the EC is given in the output $\mathbf{J}_i$

$$\mathbf{B}_{\mathrm{C}} = \frac{\mu_0}{4\pi}\mathbf{J}_s\mathbf{V}_s\mathbf{R}_k \quad (12)$$

where,

$$\begin{aligned}
\mathbf{J}_S(t) &= \left[\, skew\,(\mathbf{J}_1)\cdots \quad skew\,(\mathbf{J}_i)\cdots \quad skew\,(\mathbf{J}_n)\,\right] \\
\mathbf{V}_{\mathrm{S}} &= diag\left(v_1\mathbf{I} \quad \cdots \quad v_i\mathbf{I} \quad \cdots \quad v_n\mathbf{I}\right)
\end{aligned}$$

and

$$\mathbf{R}_k = \left[\, \mathbf{r}_{1k}^{\mathrm{T}}/r_{1k}^3 \quad \cdots \quad \mathbf{r}_{ik}^{\mathrm{T}}/r_{ik}^3 \quad \cdots \quad \mathbf{r}_{nk}^{\mathrm{T}}/r_{nk}^3 \,\right]^{\mathrm{T}}.$$

The current flowing through the EM is given by

$$\mathbf{B}_{\mathbf{E}} = \boldsymbol{\eta}_{\mathbf{E}}\mathrm{J}_{\mathrm{E}} \quad (13)$$

In Cartesian coordinates, $\eta_{\mathbf{E}}(\mathbf{r}_k)$ depends on the winding geometry

$$\eta_{\mathbf{E}}\left(\mathbf{r}_k\right) = a\left(\frac{\mu_o}{4\pi}\int_{\theta=0}^{2\pi}\int_{Z=-\rho_a}^{\rho_a}\int_{R=\rho_i}^{1}\frac{\mathbf{e}_\theta \times \left(\mathbf{r}_k - \mathbf{r}'\right)}{\left|\mathbf{r}_k - \mathbf{r}'\right|^3} R\,dR\,dZ\,d\theta\right) \quad (14)$$

For the axisymmetric coordinate, the measured MFD at any point k in the neighborhood contributed by the currents of the excitation coil $\mathbf{B}_{\mathrm{E}}$ and the eddy currents induced on the objects $\mathbf{B}_{\mathrm{C}}$ are determined by

$$\mathbf{B} - \mathbf{B}_G = \boldsymbol{\beta}_1\mathbf{J} + \boldsymbol{\beta}_2\mathbf{U} \quad (15)$$

where

$$\boldsymbol{\beta}_1 = \begin{bmatrix} \eta_{Cr1} & \cdots & \eta_{Cri} & \cdots & \eta_{Crn} \\ \eta_{\mathrm{C}z1} & \cdots & \eta_{\mathrm{C}zi} & \cdots & \eta_{\mathrm{C}zn} \end{bmatrix}$$
$$\boldsymbol{\beta}_2 = \begin{bmatrix} \eta_{Er} & 0 \\ \eta_{Ez} & 0 \end{bmatrix}$$

$\eta_{C\ell j}$ and $\eta_{E\ell}, \ell \in r, z$ are derived from Biot-Savart's law in the axis-symmetric coordinates.

The effect of the i^{th} ring element of the object υ_i is in (12), which is equivalent to the integral area of the excitation coil in the r and z directions in (15). $\mu(=\mu_0\mu_r)$ is the permeability of the conductor

$$\begin{bmatrix} \eta_{Cri} \\ \eta_{\mathrm{C}zi} \end{bmatrix} = \frac{\mu}{4\pi a_o}\int_{\theta=0}^{2\pi}\begin{bmatrix} \rho_a\,(Z_k - Z_i)\cos\theta \\ (R_i - R_k\cos\theta) \end{bmatrix}\frac{R_i v_i d\theta}{|\mathbf{R}_k - \mathbf{R}_i|^3} \quad (16)$$

$$\begin{bmatrix} \eta_{\mathrm{Er}} \\ \eta_{\mathrm{Ez}} \end{bmatrix} = \frac{\mu}{4\pi a_o}\int_{\theta=0}^{2\pi}\int_{Z=-\rho_a}^{\rho_a}\int_{\Omega_i}^{1} \times \begin{bmatrix} \rho_a\,(Z_k - Z)\cos\theta \\ (R - R_k\cos\theta) \end{bmatrix}\frac{R dR dZ d\theta}{|\mathbf{R}_k - \mathbf{R}|^3} \quad (17)$$

To account for the magnetic flux Φ_B (unit: Wb or Tm2) can be determined by integrating the $\mathbf{B}$ over a cross-sectional area $\mathbf{S}$:

$$\Phi_{\mathrm{B}} = \iint_s \mathbf{B}\cdot d\mathbf{S} \quad (18)$$

C. HARMONIC RESPONSE AND ELECTROMOTIVE FORCE OF THE SENSING COIL

The harmonic solutions to the ECD fields in (8) are given in (12), which is determined by substituting $\mathbf{J}=\mathbf{J_{Re}}+\mathrm{j}\mathbf{J_{Im}}$ into (8). $\mathbf{J_{Re}}$ and $\mathbf{J_{Im}}$ are the real and imaginary parts of $\boldsymbol{J}$. The harmonic response can be determined in (12) with specified parameters,

$$\mathbf{E}_{\mathrm{PR}} = diag\left(\mu_0 \varepsilon_{\mathrm{Re}i}\right) \tag{19a}$$

$$\mathbf{E}_{\mathrm{PI}} = diag\left(\mu_0 \varepsilon_{\mathrm{Im}i}\right) \tag{19b}$$

where ε_{Rei} and ε_{Imi} are the real and imaginary part permittivity. For the bio-material, the complex permittivity and conductivity are frequency-dependent electrical properties which can be determined by (B.1), and (B.2) using the Cole-cole dispersion.

$$\begin{bmatrix} \mathbf{J}_{\mathrm{Re}} \\ \mathbf{J}_{\mathrm{Im}} \end{bmatrix} = \begin{bmatrix} \mathbf{I} - 2\omega^2 \mathbf{E}_{\mathrm{PR}} \mathbf{A}_{\mathrm{C}} & \omega\left(\mathbf{S} + 2\omega \mathbf{E}_{\mathrm{PI}}\right) \mathbf{A}_C \\ \omega\left(\mathbf{S} + 2\omega \mathbf{E}_{\mathrm{PI}}\right) \mathbf{A}_C & 2\omega^2 \mathbf{E}_{\mathrm{PR}} \mathbf{A}_{\mathrm{C}} - \mathbf{I} \end{bmatrix}^{-1} \times \begin{bmatrix} 2\omega^2 \mathbf{E}_{\mathrm{PR}} \mathbf{A}_E \\ -\omega\left(\mathbf{S} + 2\omega \mathbf{E}_{\mathrm{PI}}\right) \mathbf{A}_E \end{bmatrix} J_E \tag{20}$$

The induced electromotive force (EMF) V_C of the sensing coil is determined by Faraday's law

$$V_C = -N_w \frac{d\Phi_{\mathrm{C}}}{dt} \tag{21}$$

where N_w is the number of turns in the sensing coil.

Divided the N_w turns into radial and axial directions with n_{sr} and n_{sz}, thus, the MF of the sensing coil Φ_C is distributed by summing the MFs from n_{sz} layers of coils and integrating elements consisting of multiple enclosing circles with n_{sr} radius. The value of MF Φ_C is divided into n_{sz} layer and summing each Φ_{Ci} layer.

$$\Phi_C = \sum_{i=1}^{n_{sz}} \Phi_{Ci} \tag{22}$$

The expression for each circle is formulated as a circle equation $X_s^2 + Y_s^2 = r_{sj}^2, j = 1, 2, \ldots n_{sr}$. Each circle can be calculated by taking the surface integral of the z-direction $\mathbf{B}_{\mathrm{C}}(\mathbf{R}_{\mathrm{k}}), k = 1, 2, \ldots N_w$ over the elements with the infinitely small sides $\mathrm{d}X_s$ and $\mathrm{d}Y_s$.

$$\Phi_{Ci} = J_E \sum_{j=1}^{n_{sy}} \int_{X_s=\pm r_{jj}} \int_{Y_s=\pm\sqrt{r_{jj}^2 - X_s^2}} \mathbf{B}_{\mathrm{C}}\left(\mathbf{R}_k\right) dY_s dX_s \tag{23}$$

With a sinusoidal current input, the MF $\Phi_{\mathrm{C}} = |\Phi_{\mathrm{C}}|\mathrm{e}^{-j\omega t}$, and using (21), the EMF can be rewritten as

$$V_C = -j\omega\Phi_C \tag{24}$$

III. NUMERICAL VERIFICATIONS AND ILLUSTRATIVE APPLICATIONS

The use of the DCS method for design analysis of the eddy current sensor can be verified with the following two focuses:

1) Numerical verification of the DCS method for the EC fields induced in biological/non-ferrous metallic objects and MFD in space, MF passing through sensing coils, and the generated EMF for the BD-EC, and MC-EC sensors.

2) Numerical validation of the sweep frequency method on the BD-EC, and MC-EC sensors for classifying different objects in biological or non-ferrous metallic objects. An example illustrates the advantages of utilizing the DCS method for the EC sensor design.

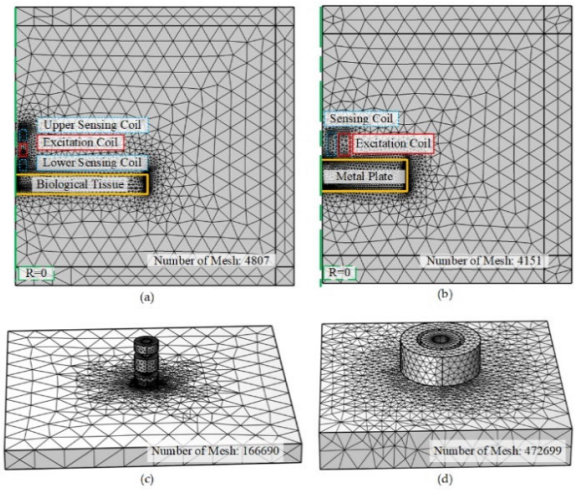

FIGURE 2. FEA Mesh. (a) 2-D axisymmetric coordinates models for BD-EC sensor. (b) ME-EC sensor. (c) 3-D Cartesian coordinates models for BD-EC sensor. (d) ME-EC sensor.

A. NUMERICAL VERIFICATION OF THE EDDY CURRENT SENSORS

The FEA verifies the DCS method in commercial software COMSOL Multiphysics. Based on the testing sample, verification is done in two parts. First, the sample is assumed to be a biological tissue with homogeneous composition. It is tested with a sensor comprised of one excitation coil in the middle and two coils winded in opposite directions. Second, an eddy current sensor model for metal samples is tested. The sensor has one excitation coil coaxial with a smaller-diameter sensing coil in the middle. Although the DCS model deals with 3D Cartesian coordinates, both setups in the frequency domain are modeled in axisymmetric coordinates in COMSOL. All the setups are axisymmetric, and thus, for comparison, only the variations in the R- and Z- directions are concerned. By simplifying the model dimension in COMSOL, the computed results are free from spatial variations in the angular direction. They are also more uniform and closer to the theoretical values. Fig. 2 shows the models for biological and metal sample sensing, along with information on the triangular mesh in 2-D axisymmetric coordinates and tetrahedron mesh in 3-D Cartesian coordinates. The excitation coils are air-cored, and the sensing coils are set to be made up of copper.

1) DIFFERENTIAL COIL SYSTEMS FOR BIOLOGICAL OBJECTS

Unlike metals, biological matters have a lower conductivity. A lower conductivity hinders the formation of eddy current and, consequently, a smaller change in MFD in the vicinity.

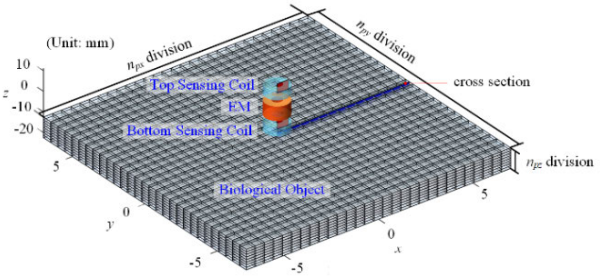

FIGURE 3. Schematics illustrating the simulation configuration of BD-EC sensor for 3-D Cartesian coordinates.

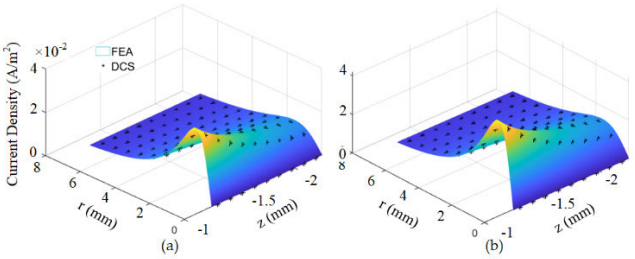

FIGURE 4. Verification of current density J of 2-D FEA and the xz-section plane in the object of the 3-D DCS model. (a) Verification of J_{Re}. (b) Verification of J_{Im}.

TABLE 2. Model parameters for biological sensing.

Excitation Coil		Sensing Coils	
a_i (mm)	2.5	a_{is} (mm)	2.5
a_o (mm)	6	a_{os} (mm)	6
a (mm)	3.5	a_s (mm)	2.25
n_E	250	(n_{sr}, n_{sz}, $n_{s\theta}$)	(10,14,10)
I (mA)	1000	d_s (mm)	0.321
f (Hz)	50k	$z_{s\pm}$(mm)	±8.75
Biological Sample (Blood)			
r_p (mm)	70	σ (S/m)	0.7008
h_p (mm)	10	ε_r	5.1977×10^3
z_p (mm)	-12.5		-2.523×10^5j
(n_{px}, n_{py}, n_{pz})	(20, 20, 4)		

This would lead to a miniature induced current in the sensing coil that is harder to detect and vulnerable to noises. A common remedy for this problem is a differential coil setup consisting of a pair of oppositely wound coils symmetric about the excitation coil, one on the top sensing coil and one at the bottom sensing coil. This setup ensures the influence from the excitation is canceled out naturally by symmetry, and the differential voltage across the two coils reveals the impact from the induced eddy current only. Fig. 3 shows the simulation configuration of the BD-EC sensor.

The excitation coil is activated by a 50kHz harmonic input signal with current 1A, and all three coils are coaxial. The middle plane of the top sensing coil situates at $z = 8.75$mm, while the bottom sensing coil sits at $z = -8.75$ mm. The lift-off distance z_p refers to the gap between the bottom sensing coil and the surface of the biological sample.

The biological object is assumed to be uniform and isotropic tissue with a conductivity of σ and a relative permittivity of ε_r. For verification purposes, the biological sample is set to be blood. There are n_{px}, n_{py}, and n_{pz} divisions in the x-, y-, and z-direction, respectively, forming a total of $(n_{px}) \times (n_{py}) \times (n_{pz})$ cells. Each of the sensing coils is equipped with sample points for calculating magnetic flux density and magnetic flux, and there are n_{sr}, n_{sz}, and $n_{s\theta}$ points in the r-, z-, and θ-direction. The use of cylindrical coordinates conforms to the shape of the sensing coils and features intuitive settings. The detailed parameters for the model can be found in Table 2.

To verify the application for sensor development, the magnetic fields in the vicinity and the EMF in the sensing coil must be in accordance with the FEA. At the inception of the excitation, eddy currents in the angular direction with a current density of **J** are induced in the biological sample. Both the induced eddy currents and the excitation contribute to the MFDs perceived by both sensing coils and the change in MFDs manifest in the EMFs in the coils. The verification for one excitation frequency f can therefore be separated into three parts: the induced current density $\mathbf{J} = \mathbf{J}_{Re} + j\mathbf{J}_{Im}$, the MFDs from both sensing coils, and finally, the EMFs flowing in the coils.

The current density **J** has only θ component with a real and an imaginary part. The comparison between the real and imaginary part eddy current fields for FEA simulations and DCS results can be found in Fig. 4(a) and Fig. 4(b), respectively. For better visual clarity and the convenience of the 2-D FEA comparison, the plate is plot the **xz**-section plane as shown in the 3D configuration of the DCS method in Fig. 3. The simulation results show that the 3-D DCS values match with the theoretical values from the 2-D FEA simulation.

From the current density flowing in the blood sample with low electrical conductivity and permittivity in 50KHz, MFDs for both top and bottom sensing coils can be computed and compared with FEA, which would be used in the calculations for EMFs. The axes of the sensing coils are perfectly perpendicular to the surface of the plate, and therefore only the z-component of the complex MFDs is concerned. The z-component MFD can be further divided into the part generated by the excitation, B_{ez}, and the eddy current-generated B_{cz}. It is worth noting that despite the inner radius of the air-cored sensing coil, the verification of the MFD covers the entire outer radius starting from $r = 0$. This is because the computation of EMF involves calculating the magnetic flux enclosed by a coil winding, which requires the knowledge of the MFD within the area encircled by the sensing coil, including the air core.

The excitation contributed B_{ez} has only a real part, for it reflects the influence of the initial input current flowing in the EM. The number of sample points for the sensing coils is increased to improve the legibility of the figures. Fig. 5(a), (b) show the identical MFD perceived by the top and bottom

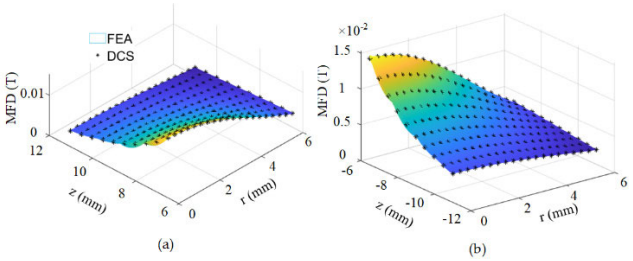

FIGURE 5. Verification of the EM-generated B_{ez}. (a) Top sensing coil. (b) Bottom sensing coil.

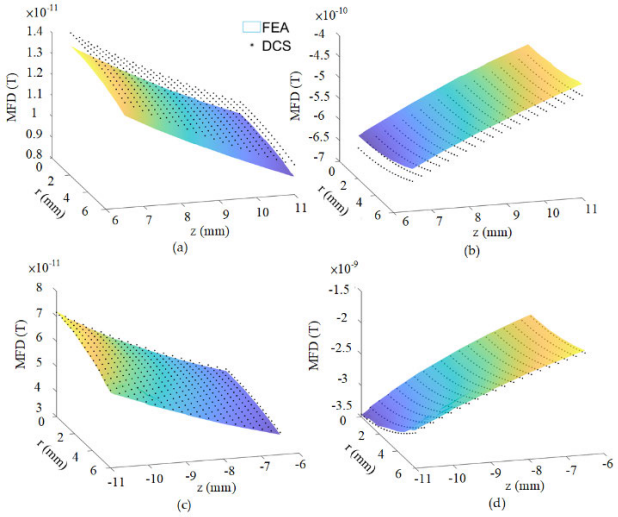

FIGURE 6. Numerical verification. (a) Real part EC-generated B_{cz} for the top sensing coil. (b) Imaginary part EC-generated B_{cz} for the top sensing coil. (c) Real part EC-generated B_{cz} for the bottom sensing coil. (d) Imaginary part EC-generated B_{cz} for the bottom sensing coil.

sensing coil for the reason of symmetrical placement. The real part of B_{ez} from COMSOL is computed by setting the sample material to air.

The MFDs contributed by the induced eddy current B_{cz} are a complex value, for the formation of the eddy currents has a phase shift from the original excitation. In COMSOL, this portion of the MFD is calculated by first obtaining the total MFD B_z and deducting the EC-generated B_{ez}. The comparisons between the DCS values and the FEA results are shown in Fig. 6.

For the top sensing coil, the magnitude of the MFDs is consistently overestimated, but the overall trend agrees with the FEA in Fig. 6(a), (b). The errors are related to the vertical distance to the object, with 5% errors. The bottom sensing coil sees a relatively consistent situation. The errors are still related to the vertical distance to the object in the z-direction. Despite the discrepancy, the overall trend still corresponds to the values from COMSOL, and the densities are ready to be used in the calculation for EMF via MF using (25). Table 3 shows the real and imaginary parts of the EMFs for both the top and bottom sensing coil. The percentage

TABLE 3. EMFs for 50kHz excitation.

	Top-sensing coil	Bottom-sensing coil
V_{Re}, DCS (V)	1.3929×10^{-5}	4.51175×10^{-5}
V_{Re}, FEA (V)	1.3179×10^{-5}	4.47108×10^{-5}
Error (%)	5.6909	0.9096
V_{Im}, DCS (V)	15.8905	15.8905
V_{im}, FEA (V)	15.6444	15.6445
Error (%)	1.5731	1.5724

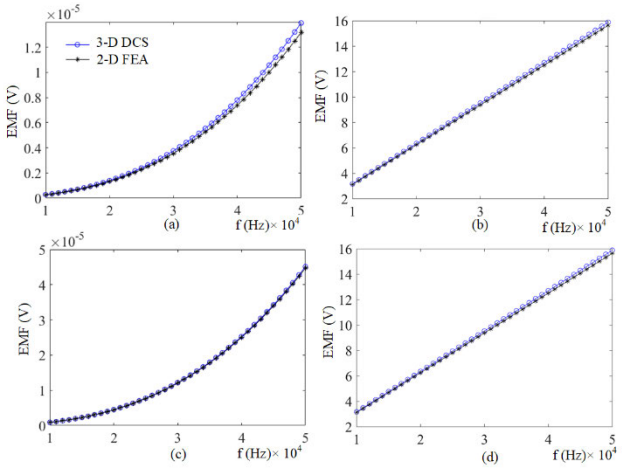

FIGURE 7. Numerical verification. (a) Real part EMF for the top sensing coil. (b) Imaginary part EMF for the top sensing coil. (c) Real part EMF for the bottom sensing coil. (b) Imaginary part EMF for the bottom sensing coil.

error is defined as

$$Error = \left| \frac{V_{\mathrm{Re},DCS} - V_{\mathrm{Re},FEA}}{V_{\mathrm{Re},FEA}} \right| \times 100\% \tag{25}$$

Once a single frequency is verified, a sweep frequency EMF computation can be performed. The frequency-dependent complex permittivity and conductivity are also altered by (B.1), and (B.2).

The errors for the real part of the EMF remain at a constant 5.6914 %, while the imaginary part of the EMF has a smaller error of 1.5731 %. The imaginary part of the EMF is largely caused by the EM-generated MFD, which explains the closer agreement with the theoretical values. On the other hand, the real part of the EMF incorporates the influence of the induced eddy currents in the plate, and the extra layer of complexity leads to a more pronounced error. Additionally, the discrepancy between the V_{Re} from the DCS method and the COMSOL simulation is more significant for the top sensing coil, which is further away from the sample. This observed phenomenon suggests that the error increases with the distance to the source of the induced eddy currents.

2) EXCITATION SENSING COIL SYSTEM FOR NON-FERROUS METALLIC OBJECTS

The electrical conductivity for the metal sample plate is several orders higher than permittivity, and eddy currents

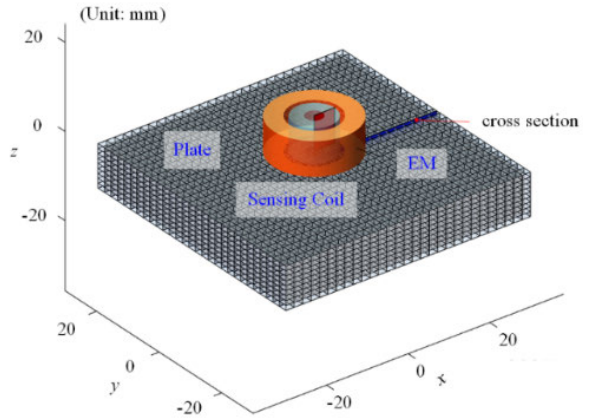

FIGURE 8. Schematics illustrating the simulation configuration of ME-EC sensor for 3-D Cartesian coordinates.

TABLE 4. Parameters for the two coil system.

Excitation Coil		Sensing Coils	
a_i (mm)	6	a_{is} (mm)	2
a_o (mm)	10	a_{os} (mm)	5
a (mm)	4	a_s (mm)	4
n_E	250	(n_{sr}, n_{sz}, $n_{s\theta}$)	(10,12,10)
I (mA)	1000	d_s (mm)	0.321
f (Hz)	50k	z_s (mm)	0
Metal Plate –Titanium be-ta-21S			
r_p (mm)	30	(n_{px},n_{py},n_{pz})	(30, 30, 10)
h_p (mm)	10	σ (S/m)	7.404×10^5
z_p (mm)	-6.5	ε_r	1

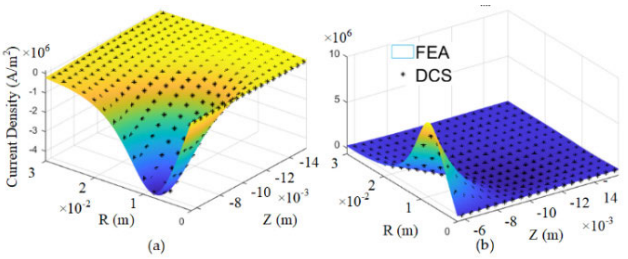

FIGURE 9. Numerical verification for the induced Eddy current density in the metal plate. (a) Real part. (b) Imaginary part.

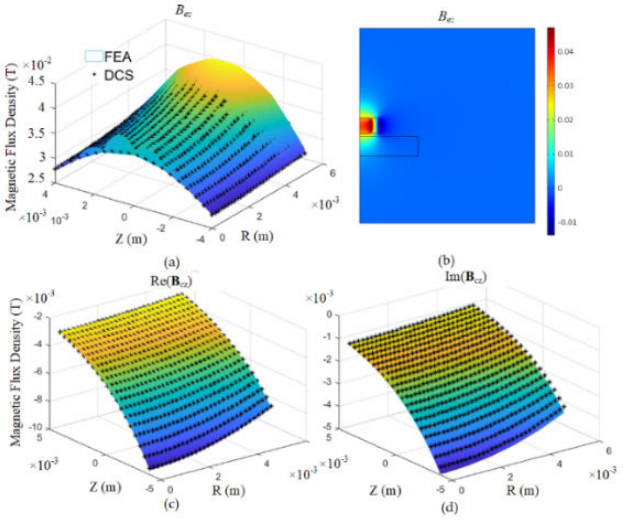

FIGURE 10. Numerical verification of the MFDs for metal sensing. (a) EM-generated B_e in the z-direction. (b) The intensity of B_z is calculated in COMSOL. (c) The real part of B_{cz}. (d) The imaginary part of B_{cz}.

forms easier in the plate. The stronger presence of eddy currents generate a larger EMF in the sensing coil. In this case, one sensing coil is enough to pick up the EMF as a result of the induced eddy currents in the plate, and by placing the sensing coil in the middle of the excitation coil, the change in MFD also cancels out due to symmetry. Model parameters are listed on Table 4, and the configuration is shown in Fig. 8.

Similar to biological settings, the verification process starts with the complex current density **J**. Fig. 9 shows that the DCS method is capable of predicting the current density distribution, even for samples with a larger electrical conductivity like Titanium material that gives rise to a larger gradient in the plate.

The MFD perceived by the sensing coil can also be separated into the EM-generated B_{ez}, which has only a real component, and the EC-generated B_{cz}, which has both a real and an imaginary part. The verification for the coaxial sensing coil MFDs is displayed in Fig. 10. The MFDs at points within the outermost layer of the coil are compared with the FEA data, including the MFDs in the volume occupied by the coil and the air core. This enables the area integration of the MFD to get the MF, whose time derivative gives clues about the induced EMF in the sensing coil. Fig. 10(c), and (d)

TABLE 5. EMFs for 50kHz excitation.

	Sensing coil	
	Real part	Imaginary part
V_{DCS} (V)	2.9207	40.2207
V_{FEA} (V)	2.8934	38.0117
Error (%)	0.9435	5.8114

show the comparisons between the FEA results and the DCS calculations, and a great level of accordance can be observed.

The overall trend agrees, and the discrepancies are less than 5%. Building upon the matched MFDs, the real and imaginary parts of the induced EMF are listed below.

Extending the successful estimation of EMF for a single frequency, a sweep frequency calculation is carried out, stretching from 20k∼50kHz. As shown in Fig. 11, the real part of the EMF, contributed mainly by the imaginary part of the MFD B_{cz} from the induced EC, follows the FEA calculations more closely, demonstrating the validity of the model. The imaginary part of the EMF reflects the impact of the real part of the MFD, consisting primarily of the influence of the excitation. Throughout the entire frequency spectrum in this range, the ratio between the DCS-calculated EMF

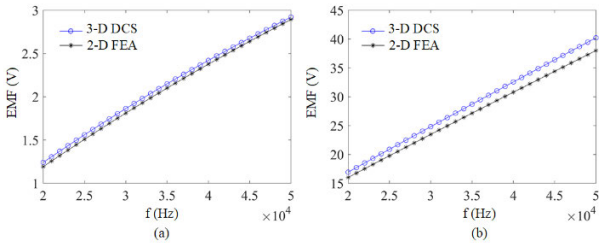

FIGURE 11. The EMF verification of the sensing coil. (a) Real part. (b) Imaginary part.

TABLE 6. Sample setups and computation time of EMF.

Sample Plate Division		
n_{px}	n_{pz}	Time (s)
30	20	1860.055235
30	4	28.816902
20	6	18.086288
30	6	64.006516
20	10	41.182380

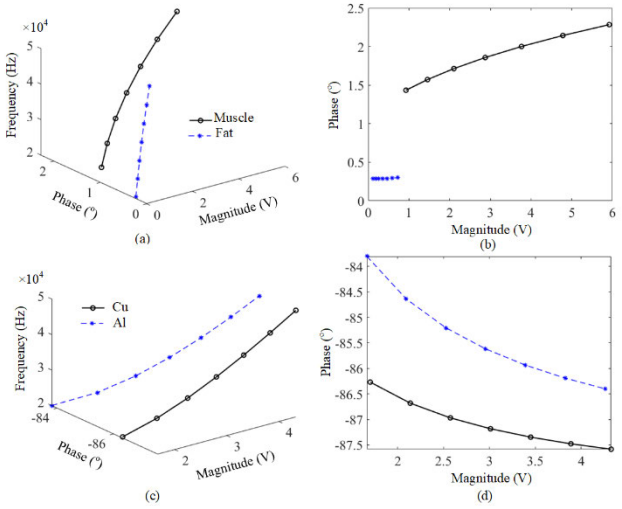

FIGURE 12. Frequency responses. (a) 3-D plots of magnitude, phase, and frequency for biological objects. (b) magnitude and phase plots for biological objects. (c) 3-D plots of magnitude, phase, and frequency for non-ferrous metallic objects (d) magnitude and phase plots for non-ferrous metallic objects.

and the FEA data remains a constant 0.95, representing a predictable error of 5% for all frequencies. The error for the imaginary part of the EMF improves with finer divisions of the metal plate, which indicates that the difference likely arises from the mesh generation for the objects.

Although raising the number of elements is a boon to accuracy, finer divisions of the objects in the model inevitably increase the processing time, and the exponential growth of the size of the square matrix poses a great challenge for the computation. The induced current densities can be depicted more accurately with more volumetric elements for the sample beneath the coils, whether a non-ferrous metallic or biological object. The calculation of MFD is not affected by the number or the placement of sample points in the sensing coil, but its density plays a major role in integrating the magnetic flux, which brings an impact on the EMF estimations, by extension. Table 6 lists several cases with different sample divisions and sample point densities for the sensing coils. The sample is set to be a square plate, and therefore the division in the y-direction n_{py} equals n_{px}.

The number of sample points in the volumetric elements in the sample has to be tuned to suit a specific setup. Generally, the higher the electrical conductivity, the larger the eddy current gradient is, which requires a denser distribution of volumetric elements. Insufficient volumetric elements would lead to a failed representation of the eddy currents with a less intense gradient, hence the number of elements used in the calculation for metal sensing. For biological application, the object has a much smaller electrical conductivity; therefore, the volumetric elements can be reduced to cut run time.

For metal sensing, a setup featuring a great balance between accuracy and run time is observed to be $n_{px} = 30$, $n_{pz} = 10$ for the plate, which is also the number used in the above verification. Owing to an eddy current distribution with a more gentle gradient, a combination of $n_{px} = 20$, $n_{pz} = 4$ is observed to be enough to capture the eddy current profile suitable for the biological application. For the sensing coils, the error for the EMF calculated with the DCS method could reach below 2% for the bottom sensing coil, which is closer to the biological sample. The results for the top sensing coil feature an error close to 5%, but the accuracy drops with the increased distance from the sample.

B. NUMERICAL VERIFICATION OF THE EXCITATION-SENSING COIL SYSTEM FOR EMF RESPONSE OF OBJECTS

The DCS method is utilized to numerically investigate the effects of applying the sweep frequency analysis on the BD-EC and MC-EC sensors to distinguish two different materials. The BD-EC and MC-EC sensors have the same geometrical configurations parameters as listed in Tables 2, 4, respectively. The frequency of the input currents is ranged from 20KHz to 50kHz. Fig. 12 (a),(b) show the simulation results of the BD-EC sensor to test the samples of muscle and fat with thicknesses of 10 mm. The dielectric spectrum is chosen by [36] and [37] to input to the Cole-Cole Dispersion model in (B.1), (B.2). Fig. 12 (c), (d) show the simulation results of applying the ME-EC sensor to test the metal sheet of Cu and Al with thicknesses 1 mm. The electrical conductivities of Cu and Al are 58.85 and 25.18 MS/m, respectively. Fig. 12(a), (c) show the 3-D magnitude, phase, and frequency plots. Fig. 12(b), (d) show the magnitude and phase plots. The simulation results demonstrate that the frequency responses of EMFs for different non-ferrous metallic and biological objects are distributed in different regions. The frequency responses of EMFs for different materials can be distinguished.

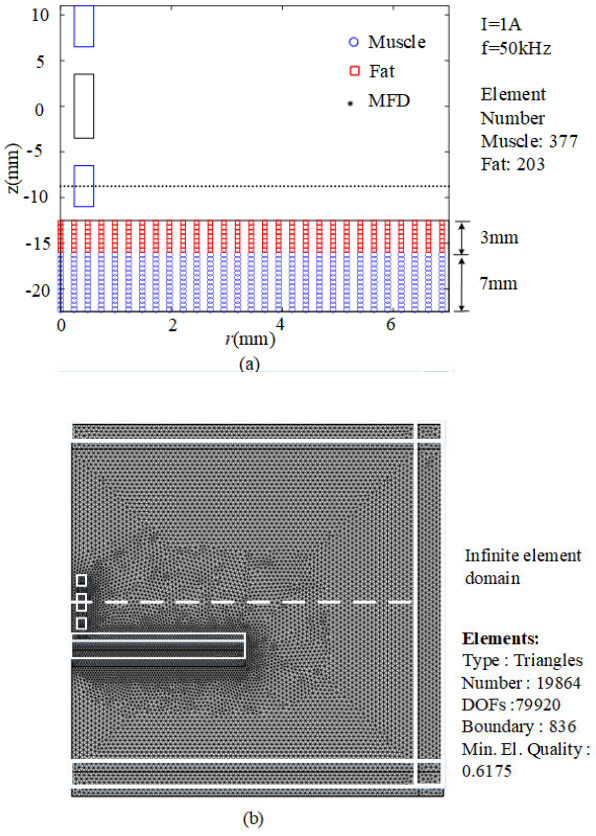

FIGURE 13. Schematics illustrating parameters used in the simulation. (a) DCS method. (b) FEA software.

Using the FEA software to calculate the magnetic field generated by the eddy currents induced in the conductor in space is to subtract the magnetic field change of the excitation coil with and without objects. Conversely, the DCS method can directly calculate the magnetic field generated by the eddy currents induced in the conductor. When the induced object is composed of multiple materials, the DCS method can calculate the magnetic field in space generated from induced eddy currents in each material by considering the coupling effects of induced eddy currents of materials, but using the FEA software can not perform this task.

The schematics of the simulation configuration of the DCS method and parametric values used in the numerical comparison are shown in Fig. 13(a). The geometry of the BD-EC sensor is the same as the values listed in Table 2. The electrical conductivities and relative dielectric constants are 0.3516, 0.0433 (S/m), and $1.0094 \times 10^4 - j1.2658 \times 10^5$, $1.6326 \times 10^2 - j1.5575 \times 10^4$ with the 50kHz input current. Fig. 13(b) shows the 2-D FEA meshes with triangular-shaped elements generated in the FEA software COMSOL.

Fig. 14 (a), (b) compare the real and imaginary parts of the ECD, and Fig. 14 (c) compares the real and imaginary parts of the z-component MFD contributed by the induced eddy currents in the conductor using the DCS method and FEA software Comsol. The comparisons between the DCS

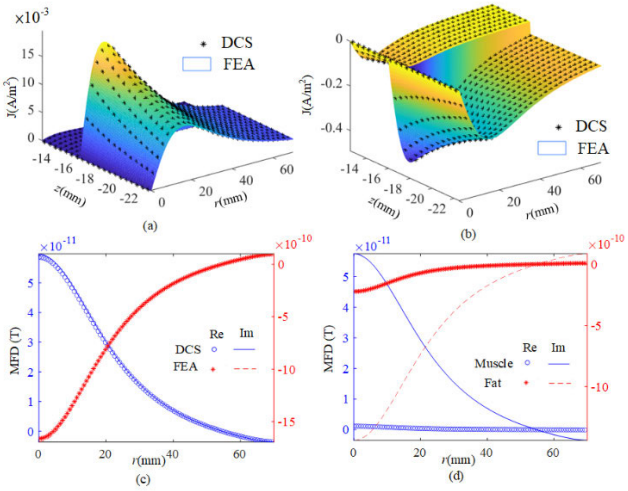

FIGURE 14. Simulation results. (a) Real part ECD. (b) Imaginary part ECD. (c) B_{cz} contributed from the biological objects. (d) B_{cz} contributed from the muscle and fat.

method and Comsol show excellent agreements. The real and imaginary parts of root-mean-square error (RMSE) are 6.4735×10^{-13} and 1.8145×10^{-11} respectively. Fig. 14(d) shows the simulated z-component MFD contributed from the muscle and fat layers individually by the DCS method, which can not be calculated using FEA software. The **RMSE** is defined as

$$RMSE = \sqrt{\frac{1}{N}\sum_{i=1}^{N}\left(B_{\mathrm{DCS},i} - B_{\mathrm{FEA},i}\right)^2} \tag{26}$$

IV. EXPERIMENTAL RESULTS AND DISCUSSIONS

The BD-EC sensor design using the proposed DCS method has been experimentally investigated. The experimental setup of the instrument, sensing probe, and biological tissue are shown in Fig. 15. The block diagram of the BD-EC sensor is shown in Fig. 15(a). The two sensing coils symmetrical to the central plane of the excitation coil are connected and wired in opposite directions to cancel out the relatively large MFD generated from the excitation coil and only detect the MFD generated from the induced ECD in the objects. The lock-in amplifier instrument is utilized to generate the input signal to the current amplifier for magnifying the current of the excitation coil. The advantage of using the lock-in amplifier is its higher resolution and precision. In the sensing system, the data acquisition system acquires the voltages of the excitation and differential sensing coils for frequency response analysis.

As shown in Fig. 15(b), the lock-in amplifier instrument was utilized to generate reference sinusoidal signals of sweeping frequency to the current amplifier to amplify the current flowing in the excitation coil. Compared reference signals with response waves of the differential sensing coil, the magnitude, and phase of the sensing system are precisely calculated by the lock-in amplifier. The NI DAQ system records the frequency response values. The lock-in amplifier

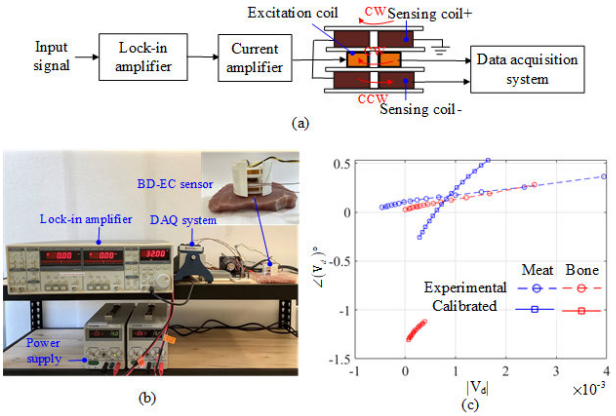

FIGURE 15. The BD-EC sensor system. (a) Block diagram. (b) Experimental setup. (c) Experimental results.

TABLE 7. Parameters for biological sensing.

Excitation Coil		Sensing Coils	
a_i (mm)	3	a_{is} (mm)	3
a_o (mm)	7.5	a_{os} (mm)	13.5
a (mm)	3.5	a_s (mm)	2.5
n_E	100	n_s	10000
d_E (mm)	0.5	d_s (mm)	0.06
I (mA)	1000	$z_{s\pm}$(mm)	±2.143
f (Hz)	20k		
Muscle		**Bone**	
r_p (mm)	5	r_p (mm)	5
h_p (mm)	8.57	h_p (mm)	2
z_p (mm)	3.286	z_p (mm)	3.286
σ (S/m)	0.3447	σ (S/m)	0.0829
ε_r	1.552×10^4-3.105×10^5j	ε_r	1.006×10^3-7.464×10^4j

and DAQ system setup are sampled at a rate of 800 kHz. The geometry of the coil probe and the detailed parameters of electrical conductivities of muscle and bone 0.3447 S/m and 0.0829 S/m at 20 kHz are listed in Table 7.

The magnitude and phase of the sensing coils are adjusted to zero by balancing the magnitude and phase of the sensor without the biological objects below the BD-EC sensor at 23.5°C ambient temperature. The transfer function $G_c(j\omega)$ in (27) was accounted to calibrate the relation between simulation and experiment that the manufacturing error of the winding misalignment of the coils and the difference of the tissue condition in the electrical conductivity between Cole-Cole dispersion and the experiment may cause. **Mc** and $\angle P_C$ are the calibrated magnitude and phase. The relationship between the calibrated magnitude and phase (M_C, $\angle P_C$) and the experimental (M_E, $\angle P_E$) and simulated (M_S, $\angle P_S$) data is determined by (28a), (28b).

$$G_C(j\omega) = M_C \angle P_C \tag{27}$$

$$M_E = M_C M_S \tag{28a}$$

$$\angle P_E = \angle P_C + \angle P_S \tag{28b}$$

M_c and $\angle P_S$ are determined by the least square estimation in (29a), (29b), where q is the number of data. The calibrated magnitude and phase $(M_C, P_C) = (4.477, -1.691°)$ are determined by the least square estimation in (29a), (29b), where m is the number of data.

$$M_C = \sum_{i=1}^{m} (M_{Ei} M_{Si}) \Big/ \sum_{i=1}^{m} M_{Si}^2 \tag{29a}$$

$$\angle P_C = \frac{1}{q} \sum_{i=1}^{m} (\angle P_{Ei} - \angle P_{Si}) \tag{29b}$$

A frequency responses test was conducted on the pork meat and pork bone using the BD-EC sensing system. Fig. 15(c) shows calibrated simulation and experimental data to apply the sweep frequency analysis on the pork meat and bone. The input frequency ranges from 20 kHz to 48 kHz. The experimental results show that both the calibrated and experimental magnitude and phase of the pork meat and bone increase as the frequency increases. For the phase response, the bone is smaller than the meat, which is caused by the lower electrical conductivity. The results show that the simulated and experimental data have the same characteristics. The magnitude of EMF increases as the frequency increases, and both phase values are tiny.

V. CONCLUSION

A DCS method for modeling the magnetic field, and eddy current fields of the biological and non-ferrous metallic objects in 2-D axisymmetric and 3-D Cartesian coordinates in state-space has been formulated. The excitation-coil-induced objects are divided into elements to calculate their induced EC field as the current source for the contribution of the magnetic field in space. The EMF of the sensing coil is with the representation of the state-space and harmonic form.

The DCS-based EC models and their applications for designing two kinds of EC sensors have been numerically illustrated: the BD-EC sensor for distinguishing biological objects and the ME-EC sensor for classifying metal. The real and imaginary parts of the 3-D DCS-generated EC and MFD match with the FEA simulation. Sweep frequency responses of EMF show great fit. The DCS-calculated EMF and the FEA data have a predictable error of 5% for all frequencies.

The advantage of the DCS method is that the MFD and EMF contributed by the induced ECD in the conductor can be directly calculated. When the excitation object is composed of multiple materials, the DCS method can calculate MFD and EMF contributed from each material. The DCS-based EC sensor design was implemented on a prototype of the BD-EC sensor to distinguish the meat and bone. The experimental results show the feasibility of applying the sweep frequency response analysis on the BD-EC sensor for distinguishing biological objects. The DCS modeling method can be adapted for a spectrum of applications for biological and metallic objects. Applications may include design analysis of EC sensing systems or EC stimulation systems, such as transcranial magnetic stimulation.

APPENDIX A
GOVERNING EQUATION OF MAGNETIC/ EDDY-CURRENTS FIELDS

Maxwell's equations which relate the magnetic and electric fields are given by (A.1)-(A.4), where **H** and **B** are the magnetic field intensity and magnetic flux density respectively. **E** and **J** are the electric field intensity and eddy current density. μ_0 is the permeability of free space. ε is the permittivity:

$$\nabla \times \mathbf{H} = \mathbf{J} \tag{A.1}$$

$$\nabla \times \mathbf{E} = -\partial \mathbf{B}/\partial t \tag{A.2}$$

$$\mathbf{B} = \mu_o \mathbf{H} \tag{A.3}$$

$$\mathbf{J} = \sigma \mathbf{E} + \frac{\partial(\varepsilon \mathbf{E})}{\partial t} \tag{A.4}$$

The magnetic vector potential (MVP) is determined by

$$\mathbf{B} = \nabla \times \mathbf{A} \tag{A.5}$$

A and **B** can be written in the integral form [29], where (A.7) is utilizing the Biot-Savart law

$$\mathbf{A}(\mathbf{r}) = \frac{\mu_0}{4\pi} \int_\Omega \frac{\mathbf{J}(\mathbf{r}')}{|\mathbf{r} - \mathbf{r}'|} dV \tag{A.6}$$

$$\mathbf{B}(\mathbf{r}) = \frac{\mu_0}{4\pi} \int_\Omega \frac{\mathbf{J}(\mathbf{r}') \times (\mathbf{r} - \mathbf{r}')}{|\mathbf{r} - \mathbf{r}'|^3} dV \tag{A.7}$$

From (A.2) and (A.5), the relationship between A and E is determined by

$$\mathbf{E} = -\frac{\partial \mathbf{A}}{\partial t} \tag{A.8}$$

From (A.4) and (A.6), **J** can be determined by

$$\mathbf{J} = -\left(\sigma + \dot{\varepsilon} + \varepsilon \frac{\partial}{\partial t}\right) \frac{\partial \mathbf{A}}{\partial t} \tag{A.9}$$

APPENDIX B
COLE-COLE DISPERSION

Frequency-dependent complex permittivity and conductivity of biological materials are given in (B.1), (B.2), where ε_0, ε_∞, ε_{Im} are the permittivity of free space, the permittivity in the high-frequency limit, and the imaginary part of relative permittivity, respectively. σ_I is the static ionic conductivity. The dielectric spectrum $\Delta\varepsilon_n$, τ_n, and α_n are chosen for each tissue described by [36] and [37].

$$\frac{\varepsilon(\omega)}{\varepsilon_0} = \varepsilon_\infty(\omega) + \sum_{n=1}^{4} \frac{\Delta\varepsilon_n}{1 + (j\omega\tau_n)^{1-\alpha_n}} - j\frac{\sigma_I}{\omega\varepsilon_0} \tag{B.1}$$

$$\sigma(\omega) = -\omega\varepsilon_{\mathrm{Im}}(\omega) \tag{B.2}$$

REFERENCES

[1] D. K. Supreeth, S. I. Bekinal, and R. C. Shivamurthy, "An overview on electrodynamic bearings," *IEEE Access*, vol. 10, pp. 57437–57451, 2022.

[2] A. Onat and S. Markon, "Theoretical and experimental analysis of eddy current contactless speed sensors for linear motor elevators," *IEEE Sensors J.*, vol. 22, no. 7, pp. 6345–6352, Apr. 2022.

[3] L. Ye, D. Li, Y. Ma, and B. Jiao, "Design and performance of a water-cooled permanent magnet retarder for heavy vehicles," *IEEE Trans. Energy Convers.*, vol. 26, no. 3, pp. 953–958, Sep. 2011.

[4] H. A. Sodano, J.-S. Bae, D. J. Inman, and W. K. Belvin, "Concept and model of eddy current damper for vibration suppression of a beam," *J. Sound Vibrat.*, vol. 288, nos. 4–5, pp. 1177–1196, Dec. 2005.

[5] H.-L. Lin, S.-C. Chen, M.-C. Jeng, P. S. Minh, J.-A. Chang, and J.-R. Hwang, "Induction heating with the ring effect for injection molding plates," *Int. Commun. Heat Mass Transf.*, vol. 39, no. 4, pp. 514–522, Apr. 2012.

[6] C. Nimonkar, E. Knight, I. C. Carmona, and R. L. Hadimani, "Development of anatomically accurate brain model of small animals for experimental verification of transcranial magnetic stimulation," *IEEE Trans. Magn.*, vol. 58, no. 2, pp. 1–4, Feb. 2022.

[7] T. A. Wagner, M. Zahn, A. J. Grodzinsky, and A. Pascual-Leone, "Three-dimensional head model simulation of transcranial magnetic stimulation," *IEEE Trans. Biomed. Eng.*, vol. 51, no. 9, pp. 1586–1598, Sep. 2004.

[8] E. M. Wassermann and S. H. Lisanby, "Therapeutic application of repetitive transcranial magnetic stimulation: A review," *Clin. Neurophys.*, vol. 112, no. 8, pp. 1367–1377, Aug. 2001.

[9] V. Chaturvedi, M. R. Nabavi, J. G. Vogel, and S. Nihtianov, "Demodulation techniques for self-oscillating eddy-current displacement sensor interfaces: A review," *IEEE Sensors J.*, vol. 17, no. 9, pp. 2617–2624, May 2017.

[10] M. R. Nabavi and S. N. Nihtianov, "Design strategies for eddy-current displacement sensor systems: Review and recommendations," *IEEE Sensors J.*, vol. 12, no. 12, pp. 3346–3355, Dec. 2012.

[11] Z. Zeng, Y. Liao, X. Liu, J. Lin, and Y. Dai, "Detection of fiber fracture in unidirectional CFRP by remote field eddy-current testing," *IEEE Trans. Instrum. Meas.*, vol. 69, no. 8, pp. 5755–5762, Aug. 2020.

[12] X. Lu, Q. Yi, and G. Y. Tian, "A comparison of feature extraction techniques for delamination of CFRP using eddy current pulse-compression thermography," *IEEE Sensors J.*, vol. 20, no. 20, pp. 12415–12422, Oct. 2020.

[13] H. Wang, W. Li, and Z. Feng, "Noncontact thickness measurement of metal films using eddy-current sensors immune to distance variation," *IEEE Trans. Instrum. Meas.*, vol. 64, no. 9, pp. 2557–2564, Sep. 2015.

[14] X. Ma, A. J. Peyton, and Y. Y. Zhao, "Measurement of the electrical conductivity of open-celled aluminium foam using non-contact eddy current techniques," *NDT E Int.*, vol. 38, no. 5, pp. 359–367, Jul. 2005.

[15] X. Li, G. Tian, K. Li, H. Wang, and Q. Zhang, "Differential ECT probe design and investigation for detection of rolling contact fatigue cracks with different orientations," *IEEE Sensors J.*, vol. 22, no. 12, pp. 11615–11625, Jun. 2022.

[16] S. Gabriel, R. W. Lau, and C. Gabriel, "A new detection method of the surface broken wires of the steel wire rope using an eddy current differential probe," *IEEE Access*, vol. 10, pp. 63619–63625, 2022.

[17] D. Tamhane, S. Banerjee, and S. Tallur, "Monitoring corrosion in sacrificial anodes with pulsed eddy current and electromechanical impedance: A comparative analysis," *IEEE Sensors J.*, vol. 22, no. 8, pp. 8147–8154, Apr. 2022.

[18] J. Jeon, C. S. Park, S. Lee, H. Y. Chae, J. J. Kim, and H. Son, "Magnetic induction tomography using multi-channel phase-domain transceiver for structural health monitoring," *IEEE Trans. Instrum. Meas.*, vol. 71, pp. 1–9, 2022.

[19] J. Xiang, Y. Dong, M. Zhang, and Y. Li, "Design of a magnetic induction tomography system by gradiometer coils for conductive fluid imaging," *IEEE Access*, vol. 7, pp. 56733–56744, 2019.

[20] M. Soleimani, "Improving the temporal resolution of magnetic induction tomography for molten metal flow visualization," *IEEE Trans. Instrum. Meas.*, vol. 59, no. 3, pp. 553–557, Mar. 2010.

[21] T. Zhang, W. Zhang, X. Liu, M. Dai, Q. Xuan, X. Dong, R. Liu, and C. Xu, "Multifrequency magnetic induction tomography for hemorrhagic stroke detection using an adaptive threshold split Bregman algorithm," *IEEE Trans. Instrum. Meas.*, vol. 71, pp. 1–13, 2022.

[22] Y. X. Chen, C. Tan, S. Zhao, and F. Dong, "Intracranial hemorrhage detection by open MIT sensor array," *IEEE Trans. Instrum. Meas.*, vol. 71, 2022, Art. no. 4500611.

[23] Y. Chen, C. Tan, and F. Dong, "Multifrequency weighted difference magnetic induction tomography for intracranial hemorrhage detection," *IEEE Trans. Instrum. Meas.*, vol. 71, pp. 1–9, 2022.

[24] J. Netz, E. Forner, and S. Haagemann, "Contactless impedance measurements by magnetic induction—A possible method for investigation of brain impedance," *Physiol. Meas.*, vol. 25, pp. 315–323, 2004.

[25] R. Casañas, H. Scharfetter, A. Altes, A. Remacha, P. Sarda, J. Sierra, R. Merwa, K. Hollaus, and J. Rosell, "Measurement of liver iron overload by magnetic induction using a planar gradiometer: Preliminary human results," *Physiol. Meas.*, vol. 25, no. 1, pp. 315–323, Feb. 2004.
[26] B. U. Karbeyaz and N. G. Gencer, "Electrical conductivity imaging via contactless measurements: An experimental study," *IEEE Trans. Med. Imag.*, vol. 22, no. 5, pp. 627–635, May 2003.
[27] C. V. Dodd and W. E. Deeds, "Analytical solutions to eddy-current probe-coil problems," *J. Appl. Phys.*, vol. 39, pp. 2829–2838, Jan. 1967.
[28] Y. Li, T. Theodoulidis, and G. Y. Tian, "Magnetic field-based eddy-current modeling for multilayered specimens," *IEEE Trans. Magn.*, vol. 43, no. 11, pp. 4010–4015, Nov. 2007.
[29] E. E. Kriezis, T. D. Tsiboukis, S. M. Panas, and J. A. Tegopoulos, "Eddy currents: Theory and applications," *Proc. IEEE*, vol. 80, no. 10, pp. 1559–1589, Oct. 1992.
[30] C.-Y. Lin, K.-M. Lee, and B. Hao, "Distributed current source method for modeling magnetic and eddy-current fields induced in nonferrous metallic objects," *IEEE/ASME Trans. Mechatronics*, vol. 23, no. 3, pp. 1038–1049, Jun. 2018.
[31] C.-Y. Lin, Y.-C. Wu, and M. Teng, "Development of a magnetic/eddy-current sensing system for simultaneous estimation of electrical conductivity and thickness in non-ferrous metal plates," *IEEE/ASME Trans. Mechatronics*, early access, Aug. 26, 2022, doi: 10.1109/TMECH.2022.3199821.
[32] O. P. Gandhi, J. F. Deford, and H. Kanai, "Impedence method for calculation of power deposition patterns in magnetically induced hyperthermia," *IEEE Trans. Biomed. Eng.*, vol. BME-31, no. 10, pp. 644–651, Oct. 1984.
[33] N. Orcutt and O. P. Gandhi, "A 3-D impedance method to calculate power deposition in biological bodies subjected to time varying magnetic fields," *IEEE Trans. Biomed. Eng.*, vol. BME-35, no. 8, pp. 577–583, Aug. 1988.
[34] N. De Geeter, G. Crevecoeur, and L. Dupré, "An efficient 3-D eddy-current solver using an independent impedance method for transcranial magnetic stimulation," *IEEE Trans. Biomed. Eng.*, vol. 58, no. 2, pp. 310–320, Feb. 2011.
[35] J. M. S. Caeiros and R. C. Martins, "An optimized forward problem solver for the complete characterization of the electromagnetic properties of biological tissues in magnetic induction tomography," *IEEE Trans. Magn.*, vol. 48, no. 12, pp. 4707–4712, Dec. 2012.
[36] K. S. Cole and R. H. Cole, "Dispersion and absorption in dielectrics I. alternating current characteristics," *J. Chem. Phys.*, vol. 9, no. 4, pp. 341–351, Apr. 1941.
[37] S. Gabriel, R. W. Lau, and C. Gabriel, "The dielectric properties of biological tissues: III. Parametric models for the dielectric spectrum of tissues," *Phys. Med. Biol.*, vol. 41, no. 11, pp. 2271–2293, 1996.

CHUN-YEON LIN (Member, IEEE) received the B.S. degree in mechanical engineering from the National Central University, Taoyuan, Taiwan, in 2003, the first M.S. degree in electrical control engineering from the National Chiao Tung University, Hsinchu, Taiwan, in 2005, the second M.S. degree in mechanical engineering from Stanford University, Stanford, CA, USA, in 2011, and the Ph.D. degree in mechanical engineering from the Georgia Institute of Technology, Atlanta, GA, USA, in 2017. He is currently an Assistant Professor with the Department of Mechanical Engineering, National Taiwan University, Taipei, Taiwan. His current research interests include mechatronics, sensors, robotics, and system dynamics and control.

MEGAN TENG received the B.S. degree in mechanical engineering and the B.B.A. degree in international business from the National Taiwan University, Taipei, Taiwan, in 2021, as a double major student. She is currently pursuing the Ph.D. degree in mechanical engineering with the University of California, Berkeley, CA, USA. She was a Research Assistant with the Department of Mechanical Engineering, National Taiwan University, from 2021 to 2022. Her current research interests include mechatronics and electromagnetic systems.

YI-CHIN WU (Graduate Student Member, IEEE) received the B.S. degree in mechanical engineering from the National Cheng Kung University, Tainan, Taiwan, in 2019, and the M.S. degree in mechanical engineering from the National Taiwan University, Taipei, Taiwan, in 2021, where he is currently pursuing the Ph.D. degree in mechanical engineering. His research interests include mechatronics and electromagnetic systems.